

See discussions, stats, and author profiles for this publication at: <https://www.researchgate.net/publication/265257418>

# Superior Long-Term Energy Retention and Volumetric Energy Density for Li-Rich Cathode Materials

ARTICLE *in* NANO LETTERS · SEPTEMBER 2014

Impact Factor: 13.59 · DOI: 10.1021/nl502980k · Source: PubMed

---

CITATIONS

11

---

READS

54

7 AUTHORS, INCLUDING:



Pilgun Oh

University of Texas at Austin

24 PUBLICATIONS 237 CITATIONS

[SEE PROFILE](#)

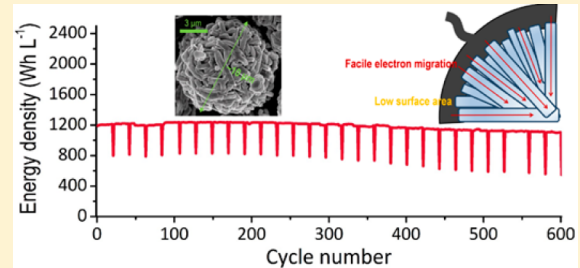
# Superior Long-Term Energy Retention and Volumetric Energy Density for Li-Rich Cathode Materials

Pilgun Oh,<sup>†</sup> Seungjun Myeong,<sup>†</sup> Woongrae Cho,<sup>†</sup> Min-Joon Lee,<sup>†</sup> Minseong Ko,<sup>†</sup> Hu Young Jeong,<sup>†,‡</sup> and Jaephil Cho<sup>\*,†</sup>

<sup>†</sup>Department of Energy Engineering, School of Energy and Chemical Engineering and <sup>‡</sup>UNIST Central Research Facilities (UCRF), Ulsan National Institute of Science and Technology (UNIST), 689-798, Ulsan, South Korea

## Supporting Information

**ABSTRACT:** Li-rich materials are considered the most promising for Li-ion battery cathodes, as high energy densities can be achieved. However, because an activation method is lacking for large particles, small particles must be used with large surface areas, a critical drawback that leads to poor long-term energy retention and low volumetric energy densities. Here we propose a new material engineering concept to overcome these difficulties. Our material is designed with 10  $\mu\text{m}$ -sized secondary particles composed of submicron scaled flake-shaped primary particles that decrease the surface area without sacrificing rate capability. A novel activation method then overcomes the previous limits of Li-rich materials with large particles. As a result, we attained high average voltage and capacity retention in turn yielding excellent energy retention of 93% during 600 cycles. This novel and unique approach may furthermore open the door to new material engineering methods for high-performance cathode materials.



**KEYWORDS:** Lithium-ion battery, Li-rich, material design, long-term cycling, chemical treatment

The fast development of portable electronic devices and electrified vehicles has increased the demand for high-energy Li-ion batteries.<sup>1–4</sup> In this regard, Li-rich materials have been considered the most promising candidates for the next generation of cathode materials.<sup>5–7</sup> In the past decade, many studies have focused on stabilizing the surfaces of these materials to overcome their intrinsically poor cycling and rate capabilities, and a number of methods, such as AlF<sub>3</sub> coating and heterostructuring, have been developed, yielding noticeable improvements.<sup>8–10</sup> Recently, however, Li-rich materials have faced new fundamental challenges with high volumetric energy densities and long-term cycle lives being required.<sup>5,11–14</sup> Because large particles lead to the partial activation of Li<sub>2</sub>MnO<sub>3</sub> phases, particle size strongly affects the reversible capacity of Li-rich materials.<sup>15–17</sup> For this reason, with large particles high voltages or multiple cycles are required to fully activate Li<sub>2</sub>MnO<sub>3</sub> phases.<sup>17–19</sup> However, these activation methods lead to their own problems, which result in degraded cell performances (Supporting Information Figure S1).<sup>20–23</sup> For this reason, secondary particle consisting of primary particles smaller than 500 nm were mostly used.<sup>9,11,12</sup> Note that the deterioration of Li-rich materials occurs through two principle mechanisms, namely side reactions with the electrolyte, and structural collapse propagating from the surface, with detrimental effects on the subsequent cycling capability. The side reactions with the electrolytes cause electrolyte exhaustion and hydrogen fluoride (HF) attack, in turn resulting over repeated cycles in the formation of unstable solid electrolyte interface (SEI) layers and in the dissolution of transition

metals.<sup>20,21,24–27</sup> On the other hand, phase transitions from layered to NiO phases, which propagate from the surface into the bulk of the material,<sup>28,29</sup> decrease the working voltage and capacity retention, severely lowering the energy density in the electrodes.<sup>11–14,30–32</sup> Accordingly, the large surface areas associated with small particles cause lower volumetric energy densities but also degrade long-term cycling performances.<sup>11,31,33–35</sup> Instead of simple surface modifications such as coating or doping, the design of new active materials is essential to overcome these limitations.

The design of new high-performance of Li-rich materials needs to start with a simple question: how can the damage from surface deteriorations be minimized on the bulk material while maximizing the volumetric energy density. The most effective answer to this question is to increase the size of the primary particles with a stable Li<sub>2</sub>MnO<sub>3</sub> activation method, because micron-sized secondary particles are used in industry.<sup>3,36,37</sup> Here we demonstrate a unique approach whereby secondary structures consisting of large flake-shaped primary particles and a novel Li<sub>2</sub>MnO<sub>3</sub> phase activation method afford extended cycle lives and a high volumetric energy density. In this design, the size and shape of the primary particles effectively reduce the surface area, in turn yielding significantly decreased surface instability with facilitated electronic conductivity, while the activation problem associated with large primary particles is

**Received:** August 4, 2014

**Revised:** August 28, 2014



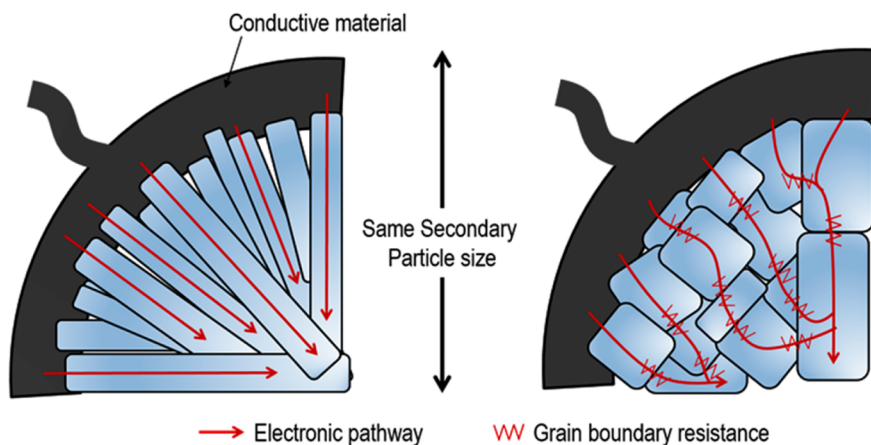


**Figure 1.** Schematic diagram showing electron migration through secondary particles composed of primary particles with different morphologies, either flake-shaped (left) or nanoparticle-shaped (right).

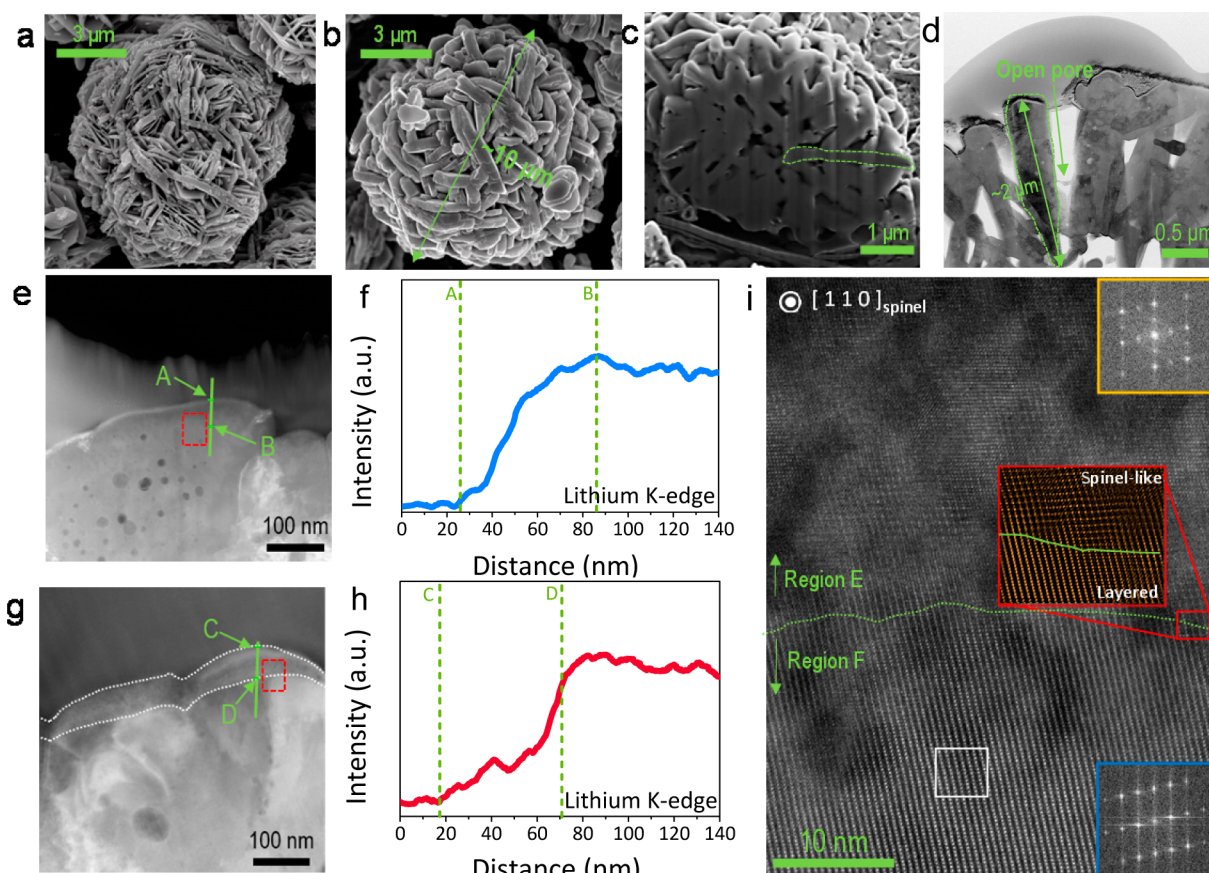


**Figure 2.** (a–c) Scanning electron micrographs of (a) the metal precursor and (b,c) the pristine material in (b) top and (c) cross-sectional views. (d,e,g) High-resolution transmission electron micrographs of (d,e) pristine and (g) F-10 samples. (f,h) Integrated Li K-edge intensity profiles from electron energy-loss spectra of the regions marked with green lines in (e) and (g) respectively. (i) High-angle annular dark-field (HAADF) image of the region enclosed by a red rectangle in (g) with insets showing the fast Fourier transform patterns of regions E (in yellow) and F (in blue). (Inset HAADF image in red rectangle in (i) indicates atomic arrangement of interface region of region E and F.)

sufficiently overcome thanks to simple chemical treatment (Figure 1).<sup>36,38–41</sup> (We refer the reader to Supporting Information Figure S1 for details of the material design.) This is the first time both a high volumetric energy density and long-term stability have been achieved for a Li-rich cathode material.

The morphologies of the  $\text{Ni}_{0.25}\text{Mn}_{0.75}(\text{OH})_2$  precursor and pristine  $0.5\text{Li}_2\text{MnO}_3\text{-}0.5\text{LiNi}_{0.5}\text{Mn}_{0.5}\text{O}_2$  (PS) are respectively

shown in Figure 2a,b. Figure 2c,d shows cross-sectional scanning electron microscopy (SEM) and transmission electron microscopy (TEM) images of the  $10 \mu\text{m}$  sized secondary particle shown in Figure 2b, made up of flake-shaped primary particles with diameters and heights in the range of  $1\text{--}3 \mu\text{m}$  and  $200\text{--}600 \text{ nm}$ , respectively. These images confirm that the surface and interior of the secondary particles are well connected through a small number of primary particles. A

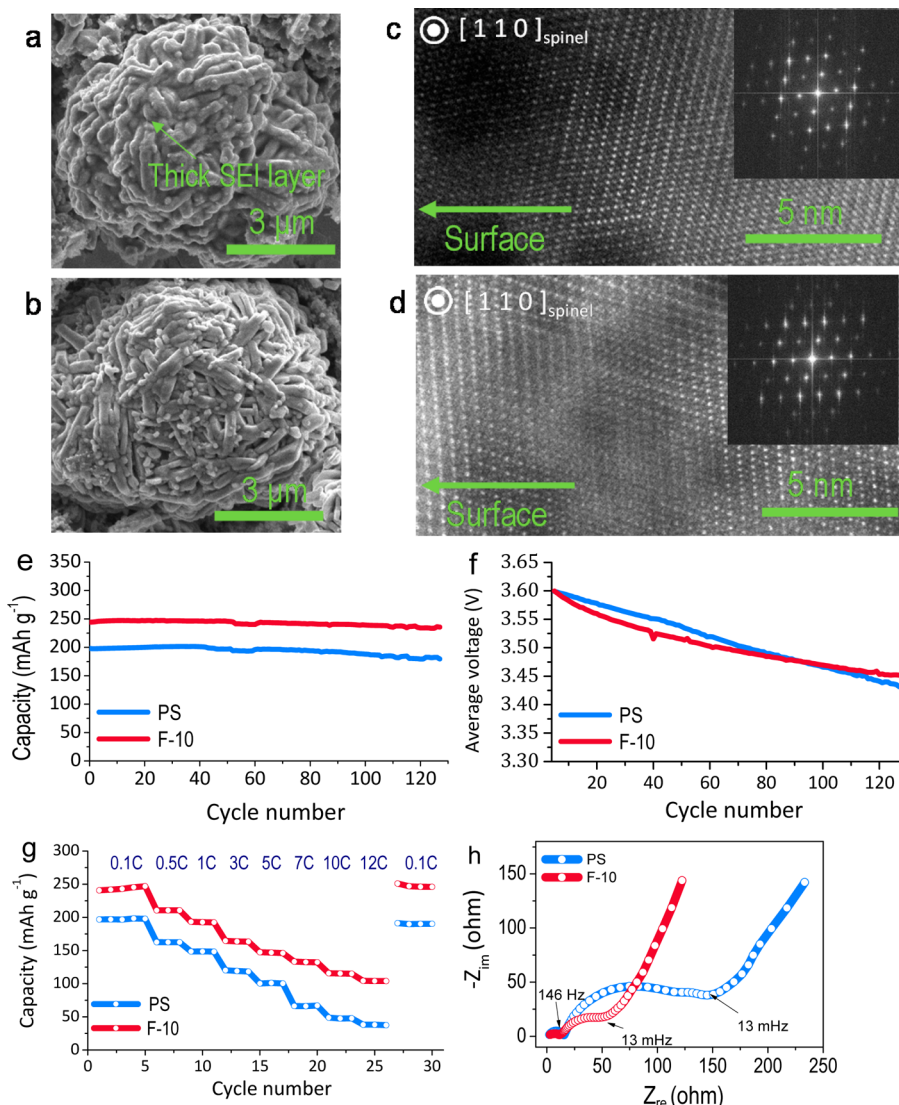


**Figure 3.** (a,b) Scanning electron micrographs of (a) PS and (b) F-10 after 5 cycles between 2.0 and 4.6 V at 0.1 C. (c,d) High-angle annular dark-field images of (c) PS and (d) F-10 after 5 cycles. (e,f) Plots of (e) discharge capacity and (f) average voltage of PS and F-10 as a function of the number of cycles between 2.0 and 4.6 V at 1 C in coin-type half-cells. (g) Rate capabilities of PS and F-10 for C-rates between 0.1 and 12 C. (h) Nyquist plots obtained from electrochemical impedance spectra of PS and F-10.

high tap density ( $2.2 \text{ g cm}^{-3}$ ) and a small surface area ( $1.2 \text{ m}^2 \text{ g}^{-1}$ ) were measured on this sample. The capacity of the PS electrode was very low initially at  $171 \text{ mAh g}^{-1}$  but increased continuously up to  $225 \text{ mAh g}^{-1}$  over 15 cycles between 2.0 and 4.65 V at 0.1 C ( $1\text{C} = 200 \text{ mA g}^{-1}$ ) (Supporting Information Figure S1). This large capacity increase results from the partial activation of the  $\text{Li}_2\text{MnO}_3$  phase due to the large particles in the pristine material. After the first 15 cycles, however, the performance of the electrode remained stable over 100 cycles at 1 C. This leads us to expect superior cycling performances for this material if the problem of partial activation were to be solved.<sup>38</sup>

An efficient activation method is essential to achieve superior electrochemical performances with large primary particles. In this case, hydrazine treatment, a chemical activation method, proved particularly effective. In Figure 2e–h, the high-resolution transmission electron spectroscopy (HR-TEM) and electron energy loss spectroscopy (EELS) images of PS and hydrazine treated PS (F-10) highlight the effects of chemical activation on the material. A darker surface layer,  $\sim 50 \text{ nm}$  thick,

is observed for F-10 (Figure 2g), which contrasts with the uniform TEM intensity obtained for PS (Figure 2e). The intensity of the Li K-edge EELS line scan integrated over the  $\sim 50 \text{ nm}$  surface layer is lower for F-10 than it is for PS, indicating a lower lithium concentration and suggesting that lithium ions are extracted from the pristine surface by hydrazine treatment (Figure 2f,h). The scanning transmission electron microscopy (STEM) image in Figure 2i, taken of the region of F-10 marked with a red rectangle in Figure 2g, highlights the structural effects of chemical activation. In contrast with the layered atomic arrangement seen throughout PS (Supporting Information Figure S2a,c,d), two distinct regions are observed for F-10, dubbed E and F. The atomic arrangement of the chemically delithiated phase in region E, differs markedly from the layered structure of region F (Supporting Information Figure S2b,f). The pattern obtained by fast Fourier transform (FFT) for region E matches that of a spinel-like phase along the spinel [110] direction (Supporting Information Figure S2e). Recently, our group reported the mechanism whereby spinel-like phases are formed on Li-rich materials during electro-

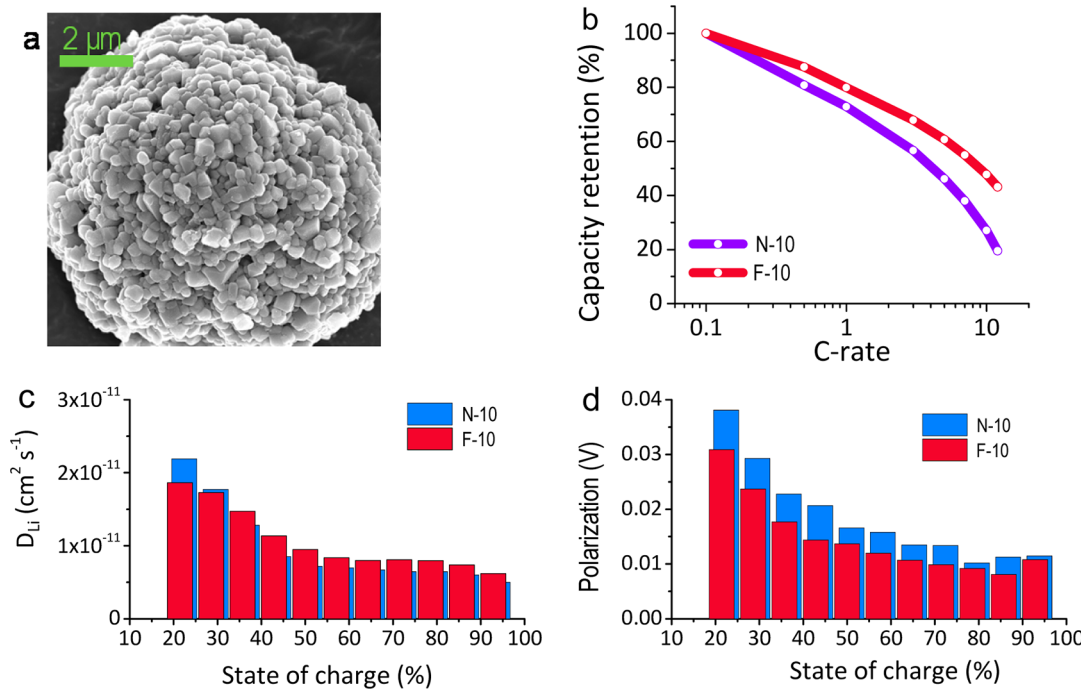


**Figure 4.** (a) Scanning electron micrograph of N-10. (b) Discharge capacity retention of N-10 and F-10 for C-rates between 0.1 and 12 C. (c,d) Plots of (c) Li diffusivity and (d) polarization calculated from galvanostatic intermittent titration technique measurements (Supporting Information Figure S5) on N-10 and F-10.

chemical cycles, namely through the migration of transition metal (TM) ions from the TM to the Li slab (Supporting Information Figure S3).<sup>28</sup> Interestingly, the chemically treated surface layer (region E) showed similar cationic disordered structure with a result of electrochemical cycles, which is spinel-like structure (Figure 2i and Supporting Information Figure S2g). The EELS result, STEM image, and the FFT pattern obtained for region E, indicate first that hydrazine treatment only activated the top  $\sim$ 50 nm of the material surface and, second, which spinel-like structure of the chemically activated region is caused by cation migration from the TM to the Li slab.

For a comparative study of chemical and electrochemical activation, different formation conditions were used for PS and F-10. The formation voltage window was 2.0–4.6 V for F-10 but 2.0–4.8 V for PS to achieve electrochemical activation at a high state of charge (SOC) (Supporting Information Figure S4a). Despite the narrower voltage window used, the initial discharge capacity obtained with F-10 ( $242 \text{ mAh g}^{-1}$ ) was higher than with PS ( $198 \text{ mAh g}^{-1}$ ). Note that a higher overpotential was measured for PS during  $\text{Li}_2\text{MnO}_3$  phase activation (above 4.5 V), while the charge profiles were similar before  $\text{Li}_2\text{MnO}_3$  activation (below 4.5 V) with the same charge capacity of  $100 \text{ mAh g}^{-1}$ . This indicates that F-10s chemically activated surface facilitated the further activation of its  $\text{Li}_2\text{MnO}_3$  phase (the evidence showing that only the  $\text{Li}_2\text{MnO}_3$  phase is activated by the chemical treatment is presented in Supporting Information Figure S4a). Furthermore, the lower discharge profile obtained for PS indicates that a large resistance was induced by the higher formation voltage of 4.8 V. To understand the origin of this resistance, PS and F-10 samples cycled 5 times between 2.0 and 4.6 V at 0.1 C after each formation cycle were compared using SEM, X-ray photo-electron spectroscopy (XPS), electrochemical impedance spectroscopy (EIS), and STEM. The SEM images of PS

show a thick surface layer after 5 cycles (Figure 3a and Supporting Information Figure S4b) that contrasts with the clean surface observed for F-10 (Figure 3b). The formation of a thick SEI surface layer on PS after 5 cycles is confirmed by the XPS results in Supporting Information Figure 4c,d. These results therefore indicate that the higher charge voltage applied to PS increases side reactions with the electrolyte resulting in the formation of a thick SEI layer on the surface.

The structural changes occurring in PS and F-10 after 5 cycles are compared in Figure 3c,d using STEM images taken along the spinel [110] direction (Supporting Information Figure S4e,f). Remarkably, FFT patterns corresponding to a spinel-like phase are obtained both for PS and F-10 after cycling, indicating similar atomic arrangements, even though the atomic structure of the two materials was different before cycling. Furthermore, Figure 3e shows that the discharge capacity retention of F-10 is better than that of PS over 130 cycles at 0.2 C. Note that in contrast with PS's result with low voltage formation cycle (Supporting Information Figure S1), the capacity of F-10 showed no increase over the initial cycles even without high voltage formation cycles, which is a strong indication that the large particles are sufficiently activated only through surface Li extraction during chemical activation. Meanwhile, both PS and F-10 showed good cycle retentions of 90.5 and 96.5%, respectively, stemming from the reduction in unstable surface area afforded by the large primary particles. Note that the transition from a layered to a spinel-like phase lowers the working voltage of Li-rich materials due to the spinel-like phase's low electrochemical reduction at below 2.9 V.<sup>11,14</sup> Therefore, the average voltage retention of Li-rich materials is an indication of the extent of this phase transition.<sup>11</sup> Despite the initial presence of spinel-like phase on its surface, the average voltage retention of F-10 (95.9% over 120 cycles, Figure 3f) compares favorably with previous studies.<sup>11,14</sup> Accordingly, we can infer from the STEM and voltage

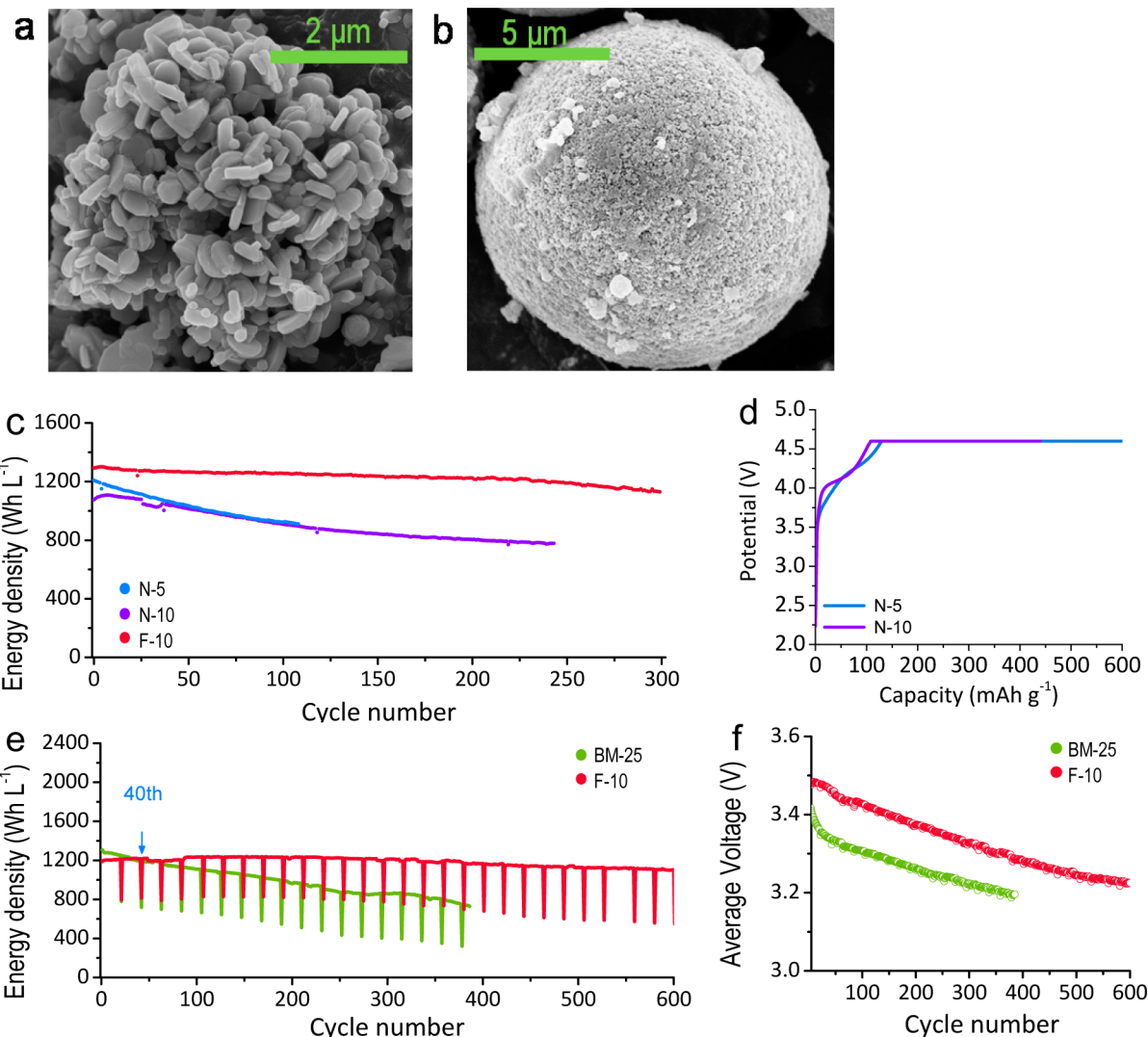


**Figure 5.** (a,b) Scanning electron micrographs of (a) N-5 and (b) BM-25. (c) Energy density of N-5, N-10, and F-10 as a function of the number of cycles between 2.0 and 4.6 V at a fixed charge/discharge rate of 1 C (constant voltage steps were applied after charging). (d) Voltage profiles of N-5 and N-10 at 110th and 240th cycle, respectively. (e) Cycling performance of F-10 and BM-25 at discharge rates of 1 C with 5 C pulse cycles (every 20 cycles). The charge rate was 0.5 C without a constant voltage step. (f) Average voltage retentions obtained with the same samples and conditions as described for (e).

retention results that the initial formation of spinel-like phase on F-10s surface has a minimal effect on the structural instability over subsequent cycles and conclude that this efficiently activated material with large particles showed superior structural maintenance.

The rate tests in Figure 3g show a clear discrepancy between the effects of electrochemical and chemical activation with F-10 having a better rate performance than PS with almost 50% capacity retention at 10 C. A similar trend is derived from the EIS results with thin film ( $R_f$ ) and a charge transfer ( $R_{ct}$ ) resistances of 11.7 and 43.8  $\Omega$  for F-10, respectively, but 12.7 and 108.6  $\Omega$  for PS.<sup>42</sup> The high electrical impedance of PS is caused by the thick SEI layer formed during high voltage charging. The conclusions from this study of the electrochemical and structural effects of chemical activation are, first, that this method provides more stable activation of micron-sized Li-rich materials than electrochemical activation and, second, that this novel activation method effectively overcomes the previous performance limits of Li-rich materials with micron-sized particles.

The rate capability of F-10 was compared with that of a reference sample (N-10), containing secondary particles  $\sim$ 10  $\mu$ m in size made up of large (300–500 nm) nanoparticles (Figure 4a) to investigate the superiority of the designed secondary structure in terms of rate performance. Figure 4b shows the capacity retention of F-10 and N-10 for increasing C-rates, highlighting F-10s improved performance. To identify the origin of this difference in rate performance, measurements using the galvanostatic intermittent titration technique (GITT) were conducted on N-10 and F-10 (Supporting Information Figure S5). Note that F-10 showed much lower ohmic resistance than N-10, but similar values for Li ion diffusivity were obtained throughout the voltage profile (Figure 4c,d).<sup>42</sup> This result suggests that N-10s large electronic resistance is induced by grain boundary resistance. Indeed, the greater number of boundaries between primary particles (grain boundaries) in N-10 impede electrons traveling from the surface to the core of the secondary particle. Furthermore, these results support the notion that Li ion conductivity in dense secondary materials depends strongly on the secondary

Table 1. Comparison of Average Particle Size and Physical Properties between Ni-5, N-10, BM-25, and F-10

	N-5	N-10	BM-25	F-10
chemical composition	$\text{Li}_{1.2}\text{Ni}_{0.2}\text{Mn}_{0.6}\text{O}_2$	$\text{Li}_{1.2}\text{Ni}_{0.2}\text{Mn}_{0.6}\text{O}_2$	$\text{Li}_{1.2}\text{Ni}_{0.15}\text{Co}_{0.07}\text{Mn}_{0.55}\text{O}_2$	$\text{Li}_{1.2}\text{Ni}_{0.2}\text{Mn}_{0.6}\text{O}_2$
primary particle size (height) × (diameter)	(~100 nm) × (~300 nm)	(300–500 nm) × (300–500 nm)	(~50 nm) × (~50 nm)	(200–600 nm) × (1–3 $\mu\text{m}$ )
secondary particle size	5 $\mu\text{m}$	10 $\mu\text{m}$	15 $\mu\text{m}$ (blended with 5 $\mu\text{m}$ )	10 $\mu\text{m}$
tap density ( $\text{g cc}^{-1}$ )	1.3	1.9	2.05	2.2
BET ( $\text{m}^2 \text{ g}^{-1}$ )	3.9	2.5	4.4	1.2

rather than the primary particle size, as mentioned in the details for material design (Supporting Information Figure S1).<sup>41</sup> Consequently, flake-shaped primary particles oriented radially efficiently reduce grain boundary resistance. Therefore, the design proposed here for cathode materials is favorable not only in terms of reduced surface areas but also in terms of excellent rate capabilities.

Recently, poor working voltage retention has been identified as one of the most critical drawbacks of Li-rich materials.<sup>5,11–14,33</sup> Because the energy of electrodes is proportional to its working voltage, this decay results in decreased energy in the electrode.<sup>14</sup> To highlight the superiority of our newly designed material in terms of long-term cycling performance, the volumetric energy retentions of F-10, N-5, N-10, and the benchmarking sample BM-25 were compared (Figures 4a and 5a,b). The morphology and physical properties of each sample are given in Table 1 with F-10 having the highest tap density and lowest surface area. N-5 and N-10 have the same chemical composition ( $\text{Li}_{1.2}\text{Ni}_{0.2}\text{Mn}_{0.6}\text{O}_2$ ) as F-10. On the other hand, BM-25, obtained by acid treatment,<sup>43</sup> has the composition  $\text{Li}_{1.2}\text{Ni}_{0.15}\text{Co}_{0.07}\text{Mn}_{0.55}\text{O}_2$ . Figure 5c shows the long-term volumetric energy density retention of cells employing N-5, N-10, and F-10 cathodes (for this comparison, all electrodes were compressed down to half their original thickness). Note that the cells prepared with N-5 and N-10 short-circuited after 110 and 240 cycles, respectively (Figure 5d). This extraordinary phenomenon is the result of metal dissolution in the cathode due to side reactions with the electrolyte occurring during cycling. Note that the side reactions lead to HF attack whereby transition metals are extracted from the cathode material.<sup>28,29</sup> The dissolved ions are then reduced on the Li metal anode and the separator, which leads to the cell short-circuiting during electrochemical cycling. Because the transition metal ions are dissolved by surface side reactions with the electrolytes, the larger surface areas of N-5 and N-10 induce faster metal dissolution in the cathode during cycling (Figure 5c and Supporting Information Figure S6d). The best energy retention, 87.5%, was obtained with F-10, corresponding to 1290  $\text{Wh L}^{-1}$  after 300 cycles at the same charge/discharge rate of 1 C, and noticeably better than the values obtained for the other samples (gravimetric and volumetric capacity retentions are shown in Supporting Information Figure S6a,b), including the acid-treated benchmarking sample, BM-25 (Supporting Information Figure S7a). Furthermore, F-10 also showed improved working voltage retention, highlighting the better structural preservation afforded by minimizing transitions to the spinel-like phase (Supporting Information Figure S6c). Although we could not suppress the inherent formation of spinel-like phase, the effect of surface instability caused by the phase transition by reducing unstable surface area was succeeded to minimize. In summary, the reduced surface area of the designed material efficiently decreases the damages from surface deteriorations of side-reaction deteriorations and

surface phase transitions. A more detailed comparison of the cycle performances of F-10 and BM-25 is shown in Figure 5e. For these tests, a 5 C discharge pulse was applied every 20 cycles to probe the structural resistance of the electrodes to high C-rates.<sup>44</sup> (A charge rate of 0.5 C rate was used without a constant voltage step.) An energy retention of 93% was measured for the F-10 cell over 600 cycles (as discussed in Supporting Information Figure S7d, the slight increase in energy density for the F-10 sample does not indicate partial activation of the  $\text{Li}_2\text{MnO}_3$  phase). In contrast, the energy retention with BM-25 was poor, namely 55% over 400 cycles, with greater deterioration under the high C-rate pulses (Figure 5e and Supporting Information Figure S7a). The structural retention of F-10 was also superior, as indicated by its extremely high voltage retention of 95.4% during 380 cycles, compared with 92.3% for BM-25 (Figure 5f). These results indicate that in contrast with BM-25 our material is highly resistant not only to low current discharge but also to rapid current densities. Meanwhile, more stable cycle performance of BM-25 despite having the highest surface area among the four samples seems to be related to the Co content in the material.

The novel design we propose increases the volumetric energy density of the electrode material by decreasing the amount of conductive active material and binder required. Figure 6

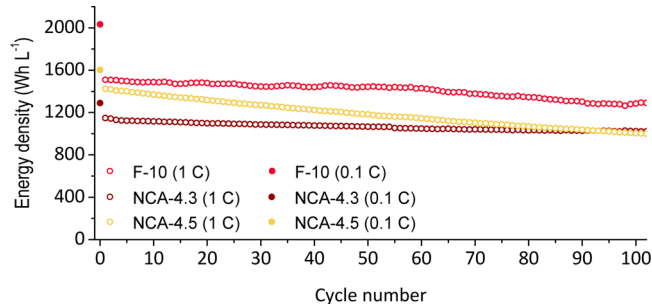


Figure 6. Energy density retention of F-10 (red circles) and NCA (black and yellow circles) as a function of the number of cycles at either 0.1 C (empty circles) or 1 C (filled circles). All electrodes consisted of active material, conductive material, and binder with a weight ratio of 90:5:5. Two different voltage conditions were used for NCA, namely 2.0–4.3 V (brown circles) or 2.0–4.5 V (yellow circles). For F-10, 2.0–4.6 V was used.

compares the volumetric energy density retentions of F-10 and commercial  $\text{LiNi}_{0.8}\text{Co}_{0.15}\text{Al}_{0.05}\text{O}_2$  material (NCA), which contains a high proportion (90%) of active material.<sup>45</sup> The tests on NCA were conducted within two voltage ranges: 2.0–4.3 V (denoted NCA-4.3) and 2.0–4.5 V (denoted NCA-4.5). The volumetric energy density of F-10, 2030  $\text{Wh L}^{-1}$  at 0.1 C, is noticeably higher than those of the other samples (gravimetric and volumetric capacity retentions are shown in Supporting Information Figure S8).<sup>35</sup> In terms of energy

retention furthermore, F-10 performs better than NCA-4.5 with 86% retention over 100 cycles, which is similar to the 88% retention of NCA-4.3. This result is noteworthy in that the energy retention of F-10 matches that of a commercially viable material but with a superior volumetric energy density. Overall therefore, the proposed material successfully overcomes the problems of poor long-term energy retention and low volumetric energy density currently associated with Li-rich materials.

In conclusion, the unique engineering method we propose, where ideal structuring is combined with efficient activation, overcomes the biggest drawbacks of Li-rich materials that are their low volumetric energy density and poor long-term energy retention, without sacrificing rate capability. The material is composed of 10  $\mu\text{m}$  sized secondary particles built with submicron-sized flake-shaped primary particles designed to have a low surface area and to facilitate electron migration. Efficient activation of the  $\text{Li}_2\text{MnO}_3$  phase was achieved with hydrazine treatment, solving the problem of partial activation, which is a critical limitation of Li-rich materials with large particles. As a result, this material showed excellent long-term energy and voltage retention over 600 cycles. Two aspects of this research are particularly significant. First, this unique approach is the first to successfully produce high-performance cathode materials using Li-rich material with large particles. Second, in contrast with previous reports in which performances were only made with pristine material, the superiority of our approach was verified in comparison with various control groups including the benchmarking sample BM-25 and commercial NCA. The novel design and the efficient surface activation lead to remarkable electrochemical results and extend our understanding of material engineering methods.

#### **Experimental Section. Preparation of Pristine Material.**

To prepare  $\text{Ni}_{0.25}\text{Mn}_{0.75}(\text{OH})_2$ ,  $\text{NiSO}_4 \cdot 6\text{H}_2\text{O}$ , and  $\text{MnSO}_4 \cdot 5\text{H}_2\text{O}$  were mixed with a molar ratio of Ni/Mn = 1:3 in distilled water at a concentration of 2.0 M. The mixed solution was transferred into a 7 L continuous stirred tank reactor (CSTR) under  $\text{N}_2$  atmosphere, and the pH was adjusted to 10 with an appropriate amount of 15.3 M  $\text{NH}_4\text{OH}$  and 4 M NaOH in order to reach the initial conditions for the reaction. Simultaneously, a metal solution was fed separately into the reactor with an aqueous solution of NaOH and  $\text{NH}_4\text{OH}$ . The total feed rate was regulated to ensure an average residence time of 8 h in the continuous stirred tank reactor kept at 50 °C. The coprecipitated particles were filtered, washed, and dried at 120 °C for 24 h to obtain  $\text{Ni}_{0.25}\text{Mn}_{0.75}(\text{OH})_2$  precursor. The prepared precursor was mixed with  $\text{LiOH} \cdot \text{H}_2\text{O}$  at a molar ratio of 1:1.5 and preheated at 450 °C for 5 h then calcined at 900 °C for 15 h to obtain  $\text{Li}_{1.2}\text{Ni}_{0.2}\text{Mn}_{0.6}\text{O}_2$  (denoted as PS). To control the morphology of the  $\text{Ni}_{0.25}\text{Mn}_{0.75}(\text{OH})_2$  precursor, the pH and temperature coprecipitation conditions were varied. A pH of 11 was used for the N-5 sample with the tank reactor kept at 60 °C under  $\text{N}_2$  atmosphere, while for N-10 coprecipitation was conducted at pH 10.5 at 50 °C in air.

**Chemical Activation.** The PS was mixed with a 0.4 wt % hydrazine solution for 3 h in a water bath at 90 °C. The resulting material (denoted as F-10) was annealed at 250 °C for 3 h.

**Structural Characterization.** To investigate differences in the crystalline phases of the samples, powder X-ray diffraction (D/MAX 2500 V/PC) was used with  $\text{CuK}\alpha$  radiation. The surface morphologies of the samples were observed by SEM (JSM 6400, JEOL). The cross-sectional TEM specimens were

prepared by Focused Ion Beam (FIB) technique (FEI Helios NanoLab 450) and were additionally thinned by a low-energy Ar-ion milling system (Fischione Model 1040 Nanomill). A field-emission electron microscope (JEM-2100F, JEOL) was used to identify differences in the surface phases of PS and the surface-modified samples at atomic resolution. Electron energy loss spectra of Li K-edge were performed using Gatan GIF Quantum 965 spectrometer equipped at Titan3 G2 60-300 microscope.

**Electrochemical Tests.** The electrochemical performances of the different samples were tested in a coin-type (2032R) half-cell with a lithium metal anode. The electrolyte was a solution of 1.15 M  $\text{LiPF}_6$  in ethylene carbonate (EC)/diethyl carbonate (DEC)/dimethyl carbonate (DMC) (3:3:4 vol %) (Panatech., Korea). The cathode electrode consisted of Super P carbon black, polyvinylidene fluoride (PVDF) binder (Solef 6020), and active material either at a weight ratio of 8:1:1 with active material loaded at 4.5–5.0 mg  $\text{cm}^{-2}$  or at a weight ratio of 90:5:5 with 6.2 mg  $\text{cm}^{-2}$  loading. For the GITT measurement, the cells were galvanostatically charged and discharged at 0.1 C rate between 2.0 and 4.6 V at 24 °C. The GITT was employed at a constant current pulse of 0.1 C rate for 40 min and then an open-circuit stands for 60 min to relax the cell voltage to the steady state. EIS was performed from 0.001 to 100 kHz frequency range using electrochemical interface system (IVIUM) on coin-type half cells at 4.3 V.

## ■ ASSOCIATED CONTENT

### **S Supporting Information**

TEM images, battery cycling data, and XPS graphs. This material is available free of charge via the Internet at <http://pubs.acs.org>.

## ■ AUTHOR INFORMATION

### **Corresponding Author**

\*E-mail: jpcho@unist.ac.kr.

### **Notes**

The authors declare no competing financial interest.

## ■ ACKNOWLEDGMENTS

This work was supported by the IT R&D program of MOTIE/KEIT (Development of Li-rich Cathode and Carbon-free Anode Materials for High Capacity/High Rate Lithium Secondary Batteries, 10046309). Financial support from MSIP (Ministry of Science, ICT&Future Planning), Korea, under the C-ITRC (Convergence Information Technology Research Center) support program (NIPA-2013-H0301-13-1009) supervised by the NIPA (National IT Industry Promotion Agency) is also greatly acknowledged.

## ■ REFERENCES

- (1) Yu, H. J.; Zhou, H. S. *J. Phys. Chem. Lett.* **2013**, *4*, 1268–1280.
- (2) Yu, H. J.; Ishikawa, R.; So, Y. G.; Shibata, N.; Kudo, T.; Zhou, H. S.; Ikuhara, Y. *Angew. Chem., Int. Ed.* **2013**, *52*, 5969–5973.
- (3) Jung, D. S.; Hwang, T. H.; Park, S. B.; Choi, J. W. *Nano Lett.* **2013**, *13*, 2092–2097.
- (4) He, P.; Yu, H. J.; Li, D.; Zhou, H. S. *J. Mater. Chem.* **2012**, *22*, 3680–3695.
- (5) Sathiya, M.; Rousse, G.; Ramesha, K.; Laisa, C. P.; Vezin, H.; Sougrati, M. T.; Doublet, M. L.; Foix, D.; Gonbeau, D.; Walker, W.; Prakash, A. S.; Ben Hassine, M.; Dupont, L.; Tarascon, J. M. *Nat. Mater.* **2013**, *12*, 827–835.

- (6) Kang, S. H.; Lu, W. Q.; Gallagher, K. G.; Park, S. H.; Pol, V. G. *J. Electrochem. Soc.* **2011**, *158*, A936–A941.
- (7) Yu, H. J.; Kim, H. J.; Wang, Y. R.; He, P.; Asakura, D.; Nakamura, Y.; Zhou, H. S. *Phys. Chem. Chem. Phys.* **2012**, *14*, 6584–6595.
- (8) Wu, F.; Li, N.; Su, Y.; Shou, H.; Bao, L.; Yang, W.; Zhang, L.; An, R.; Chen, S. *Adv. Mater.* **2013**, *25*, 3722–3726.
- (9) Sun, Y. K.; Lee, M. J.; Yoon, C. S.; Hassoun, J.; Amine, K.; Scrosati, B. *Adv. Mater.* **2012**, *24*, 1192–1196.
- (10) Zhang, X. F.; Belharouak, I.; Li, L.; Lei, Y.; Elam, J. W.; Nie, A. M.; Chen, X. Q.; Yassar, R. S.; Axelbaum, R. L. *Adv. Energy Mater.* **2013**, *3*, 1299–1307.
- (11) Zheng, J.; Gu, M.; Genc, A.; Xiao, J.; Xu, P.; Chen, X.; Zhu, Z.; Zhao, W.; Pullan, L.; Wang, C.; Zhang, J.-G. *Nano Lett.* **2014**, *14*, 2628–2635.
- (12) Zheng, J. M.; Gu, M.; Xiao, J.; Zuo, P. J.; Wang, C. M.; Zhang, J. G. *Nano Lett.* **2013**, *13*, 3824–3830.
- (13) Gu, M.; Belharouak, I.; Zheng, J.; Wu, H.; Xiao, J.; Genc, A.; Amine, K.; Thevuthasan, S.; Baer, D.; Zhang, J.-G.; Browning, N.; Liu, J.; Wang, C. *ACS Nano* **2013**, *7*, 760–767.
- (14) Bettge, M.; Li, Y.; Gallagher, K.; Zhu, Y.; Wu, Q. L.; Lu, W. Q.; Bloom, I.; Abraham, D. P. *J. Electrochem. Soc.* **2013**, *160*, A2046–A2055.
- (15) Yu, S. H.; Yoon, T.; Mun, J.; Park, S.; Kang, Y. S.; Park, J. H.; Oh, S. M.; Sung, Y. E. *J. Mater. Chem. A* **2013**, *1*, 2833–2839.
- (16) Wang, C. C.; Jarvis, K. A.; Ferreira, P. J.; Manthiram, A. *Chem. Mater.* **2013**, *25*, 3267–3275.
- (17) Lim, J.; Moon, J.; Gim, J.; Kim, S.; Kim, K.; Song, J.; Kang, J.; Im, W. B.; Kim, J. *J. Mater. Chem.* **2012**, *22*, 11772–11777.
- (18) Abe, M.; Matsumoto, F.; Saito, M.; Yamamura, H.; Kobayashi, G.; Ito, A.; Sanada, T.; Hatano, M.; Ohsawa, Y.; Sato, Y. *Chem. Lett.* **2012**, *41*, 418–419.
- (19) Xiang, Y. H.; Yin, Z. L.; Zhang, Y. H.; Li, X. H. *Electrochim. Acta* **2013**, *91*, 214–218.
- (20) Li, X. B.; Xu, M. Q.; Chen, Y. J.; Lucht, B. L. *J. Power Sources* **2014**, *248*, 1077–1084.
- (21) Hy, S.; Felix, F.; Rick, J.; Su, W.-N.; Hwang, B. *J. Am. Chem. Soc.* **2014**, *136*, 999–1007.
- (22) Lee, K. T.; Jeong, S.; Cho, J. *Acc. Chem. Res.* **2013**, *46*, 1161–1170.
- (23) Yu, C.; Li, G. S.; Guan, X. F.; Zheng, J.; Luo, D.; Li, L. P. *Phys. Chem. Chem. Phys.* **2012**, *14*, 12368–12377.
- (24) Yabuuchi, N.; Yoshii, K.; Myung, S. T.; Nakai, I.; Komaba, S. *J. Am. Chem. Soc.* **2011**, *133*, 4404–4419.
- (25) Martha, S. K.; Nanda, J.; Veith, G. M.; Dudney, N. J. *J. Power Sources* **2012**, *216*, 179–186.
- (26) Martha, S. K.; Nanda, J.; Kim, Y.; Unocic, R. R.; Pannala, S.; Dudney, N. J. *J. Mater. Chem. A* **2013**, *1*, 5587–5595.
- (27) Hong, J.; Lim, H. D.; Lee, M.; Kim, S. W.; Kim, H.; Oh, S. T.; Chung, G. C.; Kang, K. *Chem. Mater.* **2012**, *24*, 2692–2697.
- (28) Oh, P.; Ko, M.; Myeong, S.; Kim, Y.; Cho, J. *Adv. Energy Mater.* **2014**, DOI: 10.1002/aenm.201400631.
- (29) Lee, J.; Urban, A.; Li, X.; Su, D.; Hautier, G.; Ceder, G. *Science* **2014**, *343*, 519–522.
- (30) Mohanty, D.; Sefat, A. S.; Kalnaus, S.; Li, J. L.; Meissner, R. A.; Payzant, E. A.; Abraham, D. P.; Wood, D. L.; Daniel, C. *J. Mater. Chem. A* **2013**, *1*, 6249–6261.
- (31) Song, B. H.; Liu, Z. W.; Lai, M. O.; Lu, L. *Phys. Chem. Chem. Phys.* **2012**, *14*, 12875–12883.
- (32) Boulineau, A.; Simonin, L.; Colin, J. F.; Canevet, E.; Daniel, L.; Patoux, S. *Chem. Mater.* **2012**, *24*, 3558–3566.
- (33) Li, Y.; Bettge, M.; Polzin, B.; Zhu, Y.; Balasubramanian, M.; Abraham, D. P. *J. Electrochem. Soc.* **2013**, *160*, A3006–A3019.
- (34) Gao, M.; Lian, F.; Liu, H. Q.; Tian, C. J.; Ma, L. L.; Yang, W. Y. *Electrochim. Acta* **2013**, *95*, 87–94.
- (35) Zheng, H. H.; Li, J.; Song, X. Y.; Liu, G.; Battaglia, V. S. *Electrochim. Acta* **2012**, *71*, 258–265.
- (36) Lee, S.; Cho, Y.; Song, H. K.; Lee, K. T.; Cho, J. *Angew. Chem., Int. Ed.* **2012**, *51*, 8748–8752.
- (37) Kong, J. Z.; Yang, X. Y.; Zhai, H. F.; Ren, C.; Li, H.; Li, J. X.; Tang, Z.; Zhou, F. *J. Alloys Compd.* **2013**, *580*, 491–496.
- (38) Liu, J.; Chen, H.; Xie, J.; Sun, Z.; Wu, N.; Wu, B. *J. Power Sources* **2014**, *251*, 208–214.
- (39) Park, M.; Zhang, X. C.; Chung, M. D.; Less, G. B.; Sastry, A. M. *J. Power Sources* **2010**, *195*, 7904–7929.
- (40) Moriwake, H.; Kuwabara, A.; Fisher, C. A. J.; Huang, R.; Hitosugi, T.; Ikuhara, Y. H.; Oki, H.; Ikuhara, Y. *Adv. Mater.* **2013**, *25*, 618–622.
- (41) Wang, D. P.; Belharouak, I.; Zhou, G. W.; Amine, K. *Adv. Funct. Mater.* **2013**, *23*, 1070–1075.
- (42) Son, Y.; Park, M.; Son, Y.; Lee, J.-S.; Jang, J.-H.; Kim, Y.; Cho, J. *Nano Lett.* **2014**, *14*, 1005–1010.
- (43) Kang, S. H.; Thackeray, M. M. *J. Electrochem. Soc.* **2008**, *155*, A269–A275.
- (44) Li, J.; Klopsch, R.; Stan, M. C.; Nowak, S.; Kunze, M.; Winter, M.; Passerini, S. *J. Power Sources* **2011**, *196*, 4821–4825.
- (45) Jo, M.; Noh, M.; Oh, P.; Kim, Y.; Cho, J. *Adv. Energy Mater.* **2014**, DOI: 10.1002/aenm.201301583.